nature materials

Article

https://doi.org/10.1038/s41563-026-02568-9

Tuning phonon transmission via single-atom substituents

Received: 4 August 2025

Accepted: 6 March 2026

Yuxuan Luan[1,4], **Matthias Blaschke**[2,4], **Yuji Isshiki**[1], **Jian Guan**[1], **Fabian Pauly**[2]✉, **Edgar Meyhofer**[1]✉ & **Pramod Reddy**[1,3]✉

Thermal transport plays a crucial role in many modern electronic, photonic and energy conversion devices. Recent work has provided fundamental insights into the effects of nanostructuring on heat transport. However, the atomic-scale control of phonon transport has barely been explored. Here we present systematic studies of thermal transport in molecular junctions at 77 K, enabled by high-resolution cryogenic-compatible calorimetric scanning probes developed in this work. Our experiments provide direct evidence that atomistic changes to molecular junctions, implemented by substituting an individual hydrogen atom by a halogen atom (–F, –Cl, –Br, –I), tune the thermal conductance of the junctions by a factor of two. Our detailed first-principles modelling elucidates how the interaction between the vibrational eigenmodes of molecular junctions is modified by atomic substituents, resulting in both suppression of resonances and creation of antiresonances in the phonon transmission function. Further, the advances reported here and insights from this work inform how thermal transport in molecular materials can be probed and controlled.

Controlling phonon transport is critical for enhancing the performance and reliability of a variety of modern computing and energy conversion devices[1]. A large amount of recent work[2–5] has explored how phonon transport can be tuned by nanostructuring materials and devices with nanometre-scale modifications. Given recent advances in molecular electronics[6–8], two-dimensional (2D) molecular materials[9,10] (covalent organic frameworks) and metal–organic frameworks[11,12] (metal clusters bridged by organic molecules), where molecules form linker blocks, the following key question has arisen: can single-atom changes to the molecular building blocks, by substituting a lighter atom with a heavier one, be used to control thermal transport? Although recent theory has begun exploring this question[13–16], so far, to the best of our knowledge, no experiment has successfully probed how phonon transport can be tuned by individual atomic substituents.

Molecular junctions (MJs), created by trapping individual molecules between electrodes[6–8,17–27], are ideal systems for addressing this question, as they feature nanometric dimensions and enable atomic-scale control of the device structure. In fact, previous work has explored the effect of length[17] and isomerism[22] (molecules with the same molecular formula but different structures) on the thermal conductance of single-molecule junctions. Here, using a custom-developed experimental platform, we overcome serious experimental limitations of past work[17,18,22] and show how heat transport can be tuned and controlled by individual atomic substituents in MJs. In Fig. 1a, we schematically describe why individual substituents are expected to tune phonon transmission in MJs. Consider the spring–mass system shown in Fig. 1a with a geometry analogous to an MJ (Fig. 1a, red dashed box). The transmission of such a system, defined as the ratio of the square of the output to input oscillation amplitudes, is expected to show clear peaks at frequencies corresponding to resonances of the structure (Fig. 1a, red curve). Replacing one of the light masses (Fig. 1a, blue dashed box) with a heavier mass, to mimic the effect of single-atom substitution, is expected to suppress the resonances or introduce an antiresonance, as schematically represented by the blue and brown curves in Fig. 1a (right). These anticipated changes suggest that adding atomic substituents can strongly modify phonon

---

[1]Department of Mechanical Engineering, University of Michigan, Ann Arbor, MI, USA. [2]Institute of Physics and Center for Advanced Analytics and Predictive Sciences, University of Augsburg, Augsburg, Germany. [3]Department of Materials Science and Engineering, University of Michigan, Ann Arbor, MI, USA. [4]These authors contributed equally: Yuxuan Luan, Matthias Blaschke. ✉e-mail: fabian.pauly@uni-a.de; meyhofer@umich.edu; pramodr@umich.edu

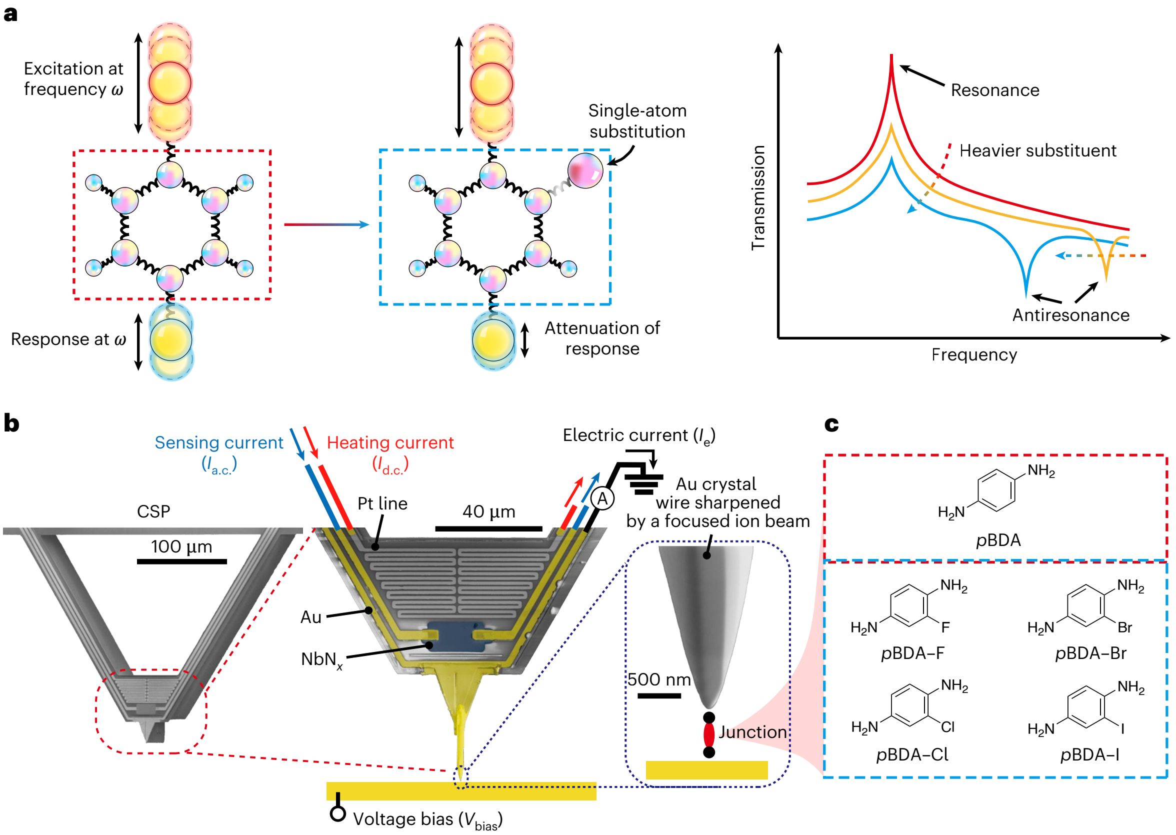

Fig. 1 | Experimental approach for exploring the effect of single-atom substitutions on thermal transport. **a**, Simplified spring–mass model and the associated transmission functions (right) schematically represent the expected changes in transmission (suppression of resonances or introduction of antiresonances) due to substituents. **b**, CSP (false-coloured scanning electron microscopy image) enables the simultaneous measurements of electrical and thermal conductances of single-atom and single-molecule junctions. The right inset shows a scanning electron microscopy image of the CSP with a sharp gold tip. **c**, Molecules used to systematically investigate the influence of substituents on the thermal transport of MJs.

transmission at specific frequencies and enable the control of heat transfer via single-atom manipulation.

To systematically explore the impact of atomistic substituents on heat transfer, we built on recent advances[17,18,28] and nanofabricated calorimetric scanning probes (CSP; Fig. 1b, left) that consist of a suspended region, which was thermally isolated from the environment. Further, a platinum (Pt) heater and a niobium nitride (NbN_x) thermometer were integrated into the suspended region (Methods and Supplementary Figs. 1–5 show the details of probe fabrication and thermal characterization). Next, to the distal end of the probe, we attached a single-crystal gold (Au) wire that was sharpened, using a focused ion beam, to feature an ~10-nm tip radius (Fig. 1b). We note that the NbN_x temperature sensor[29–31] has a much higher temperature coefficient of resistance (approximately −2% K^{-1} at 77 K) than Pt thermometers (~0.3% K^{-1} at 77 K), enabling almost an order-of-magnitude improvement in the calorimetric resolution for thermal measurements at cryogenic temperatures. Below, we describe our studies of thermal transport (at liquid-nitrogen temperature—77 K) for a series of molecules (Fig. 1c), where a hydrogen atom is systematically replaced by halogen atoms of increasing mass, to elucidate how single-atom substituents control heat transfer in MJs.

Experimental techniques

To create single-molecule junctions, we introduced CSPs and Au substrates, coated with the desired molecules (Supplementary Section 1 provides details of how the molecules were assembled onto the Au substrate), into an ultrahigh-vacuum cryogenic scanning probe microscope (Createc) and adapted the well-established scanning tunnelling microscope break junction method[8] that enables the repeatable formation of single-Au-atom junctions and single-molecule junctions. To elaborate, we first initiated physical contact between the Au tip of the probe and the molecule-decorated Au substrate to form Au atomic junctions. Then, we slowly withdrew the probe from the substrate to break the Au atomic junctions. This well-established scanning tunnelling microscope break junction approach enables the trapping of single molecules between the tip and the substrate after the single-atom Au junction ruptures (Fig. 2b (top) and Methods). To identify single-molecule junctions, we continuously monitored the electrical conductance (G_e) of the junction during the withdrawal process by applying a small a.c. electric voltage bias (V_{bias} = 5 mV at 1,001 Hz; Methods and Supplementary Section 4). The thermal conductance of the MJ was simultaneously measured by applying a temperature differential between the probe tip and the Au substrate by supplying a d.c. current of ~110 µA to the Pt line, integrated into the probe, that raised the temperature (T_p) of the suspended region by ~30 K (that is, the probe temperature was ~107 K). As the probe was withdrawn from the substrate, the temperature change of the probe (ΔT_p) was monitored via the NbN_x thermometer by supplying a small a.c. current (Methods and Supplementary Section 4). The measured ΔT_p and the known thermal resistance of the probe ($R_{th,probe}$) allowed us to quantify the thermal conductance (G_{th}) of the junction (Fig. 2a and Methods show the thermal resistance network).

Experimental study of thermal transport in MJs

We first measured the electrical and thermal conductances of MJs made from 1,4-benzenediamine (*p*BDA; Fig. 1c). Representative traces of

https://doi.org/10.1038/s41563-026-02568-9

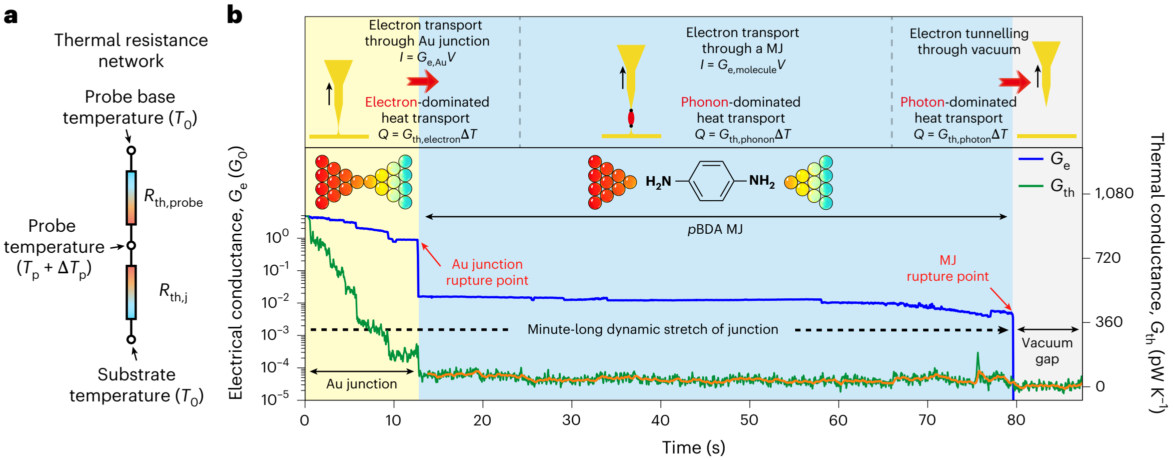

Fig. 2 | Measurements of thermal and electrical conductances of single-atom Au junctions and single-molecule junctions using a break junction method. **a**, Thermal resistance network where $R_{th,j}$ and $R_{th,probe}$ represent the thermal resistances of the junction and probe, respectively. For thermal measurements, T_p was elevated to ~107 K, and T_0 was 77 K. **b**, Representative trace showing the time evolution of the electrical and thermal conductances of a Au–*p*BDA–Au junction during a minute-long stretching process. The solid orange line represents the low-pass-filtered (~15 Hz) thermal conductance trace.

the obtained electrical conductance (G_e) and thermal conductance (G_{th}) are shown in Fig. 2b in units of G_0 ($2e^2/h \approx 77.6$ μS) and picowatt per kelvin, respectively. Here *e* is the elementary charge and *h* is the Planck constant. Evidently, the blue curve, corresponding to G_e, shows large steps associated with the rupture of Au–Au junctions and Au–*p*BDA–Au junctions (Fig. 2b indicates the rupture points). The G_{th} trace shows a thermal conductance reduction concomitant with the electrical conductance changes associated with the rupture of the Au atomic junction and the single-molecule junction. Strikingly, the G_{th} traces feature an effectively zero-background thermal conductance (that is, no background thermal conductance is detected within the experimental uncertainty). This extremely low background thermal conductance (<1 pW K^{-1}, which is much smaller than the thermal conductance of a single-molecule junction) is achieved by suppressing parasitic contributions (for example, contamination, near-field radiation) to heat transfer (Methods and Supplementary Sections 1 and 6 show the details of how this pristine thermal background is achieved). We note that eliminating these parasitic contributions is an important breakthrough as they pose a major challenge for highly precise thermal measurements[32]. Specifically, our background conductances are substantially smaller than those of past studies[17,18,22,33], which all show values that are typically >100 pW K^{-1} and are, thus, much larger than the thermal conductance of a single-molecule junction (on the order of 10 pW K^{-1}). These advances enable us to achieve information regarding the stretch dependence of thermal conductance of SMJs, as revealed in Figs. 2b, 3a,b and 4a, which was not possible before.

To unambiguously identify the thermal conductance of the Au–*p*BDA–Au junction, we used G_{th} traces from ~300 individual measurements, which featured an abrupt change in the electrical conductance corresponding to the rupture of the MJ, which enabled us to align the G_{th} data to obtain an averaged curve with a high signal-to-noise ratio (Fig. 3a and Supplementary Section 5). The data from this analysis (called rupture point analysis) show a clear thermal conductance change when the Au–*p*BDA–Au junctions rupture, implying that the (average) thermal conductance of the Au–*p*BDA–Au junction at cryogenic temperatures (92 K) is ~18.4 pW K^{-1}. We note that the observed tail in the thermal conductance trace after the rupture point arises from the settling time associated with our thermal measurements (Supplementary Section 7 shows the characterization of settling time). Given the slower response time of the thermal measurements relative to the electrical measurements, we cannot categorically rule out that some molecules in the junction that are electrically insulating but thermally conducting contribute transiently to the recorded thermal conductance signature after rupture. However, there is no detectable evidence for this in our recordings as the exponential decay in the thermal signal exactly matches the settling time of our electronic circuitry (Supplementary Section 7). We note that a small monotonic decrease in thermal conductance, as a function of stretching, is observed before the junction breaks. This behaviour, which is now observable for the first time in experiments, is consistent with our computational results (Supplementary Fig. 27).

To strengthen the above conclusions, we performed a separate histogram analysis of the data by constructing 2D histograms (Fig. 3c) that combine ~1,500 electrical and thermal conductance traces, which feature either an abrupt or gradual change in electrical conductance (Methods and Supplementary Sections 5 and 6 show a less stringent criterion than that used for the rupture point analysis). We also constructed one-dimensional (1D) histograms for electrical and thermal conductances from the 2D histogram by projecting the data onto the top and left axes in Fig. 3c. The resulting 1D histograms identify the most probable electrical and thermal conductances of the Au–*p*BDA–Au junctions (Fig. 3c, blue and red arrows in the 1D histograms), which are $2.1 \times 10^{-3} G_0$ and 19.1 pW K^{-1}, respectively. This analysis suggests that the single-molecule thermal conductances obtained from the two different analysis approaches (18.4 pW K^{-1} for the rupture point analysis versus 19.1 pW K^{-1} for the histogram analysis) are within 1 pW K^{-1}, highlighting the robustness of the measurements. We note that the measured electrical conductance ($2.1 \times 10^{-3} G_0$) of the Au–*p*BDA–Au junctions is in close agreement with the values reported in previous work[34,35]. Given this electrical conductance, the electronic contribution to thermal conductance is estimated to be <1 pW K^{-1} from the Wiedemann–Franz law[36], suggesting that in these MJs, heat transport is dominated by phonons. We also note that distinct from all past work[17,18,22,33], the measurement of thermal conductance of single-molecule junctions in this work is completely independent from the electrical conductance measurement as the presented histogram analysis does not require the identification of junction rupture point, which—in past work—is determined from the sharp drop in the measured electrical conductance. This advancement makes it possible to now probe thermal transport in single-molecule junctions, which are highly electrically resistive as the simultaneous measurement of electrical resistance is not required for thermal measurements.

https://doi.org/10.1038/s41563-026-02568-9

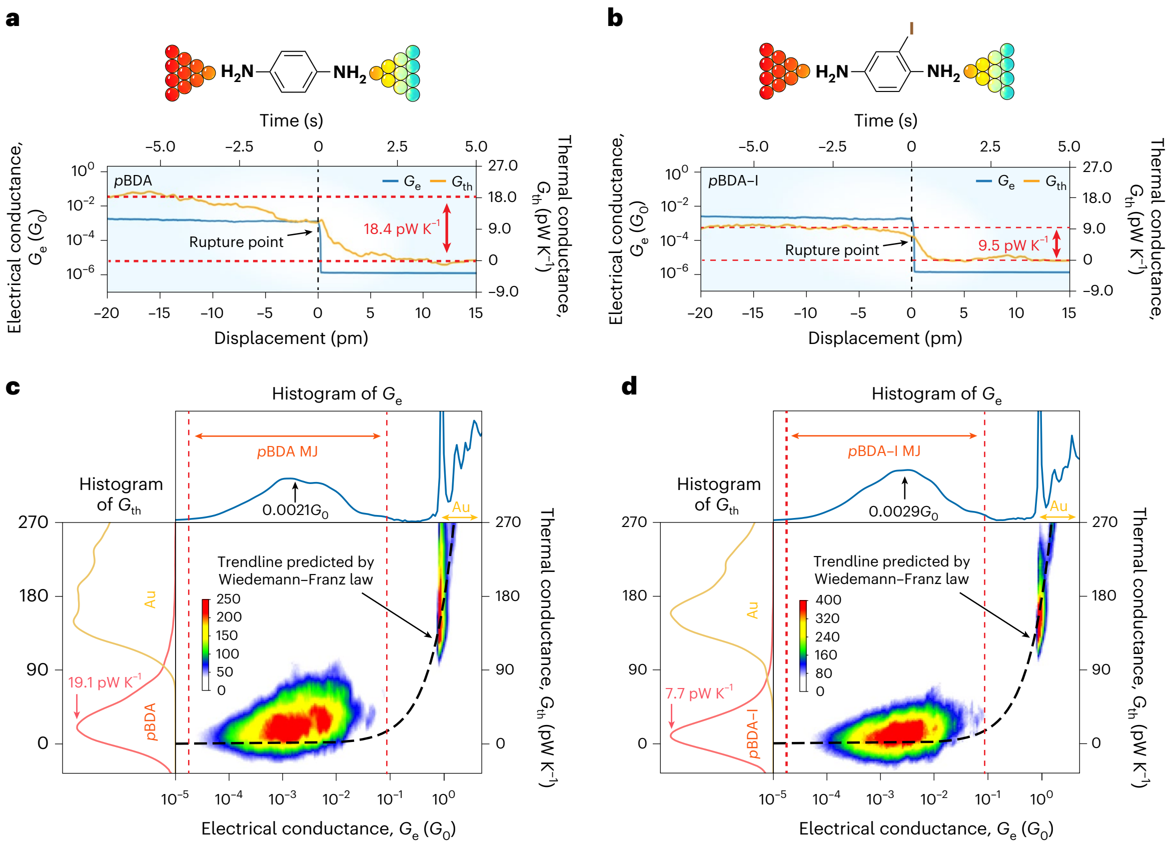

Fig. 3 | Analysis of thermal and electrical transport properties of single-molecule junctions. a,**b**, Averaged change in electrical (G_e) and thermal (G_{th}) conductances before and after the rupture of *p*BDA junctions (**a**) and *p*BDA–I junctions (**b**). **c**,**d**, 2D histograms constructed from ~1,500 measured G_e and G_{th} traces of *p*BDA (**c**) and *p*BDA–I (**d**) MJs. The corresponding 1D histograms of electrical and thermal conductances are obtained by projecting the data onto the left and top axes of the 2D histograms, respectively.

Effect of substituents on thermal transport of *p*BDA-derived junctions

Next, we performed a series of measurements using halogen-substituted *p*BDA molecules (Fig. 1c shows the molecular structures) to understand the effect of single-atom exchange on the thermal transport properties of MJs. The results from the measurements performed with iodine-substituted *p*BDA junctions (*p*BDA–I) are shown in Fig. 3b,d. The data show that on adding an iodine atom, the thermal conductance of the substituted junction is reduced to ~9.5 pW K^{-1} (Fig. 3b) and ~7.7 pW K^{-1} (Fig. 3d). Results from similar experiments, performed on a group of systematically selected molecules with F, Cl and Br substituents, are shown in Fig. 4a, and the corresponding 2D histograms are displayed in Supplementary Figs. 10–12. The electrical and thermal conductances, obtained from all these measurements, are summarized in Fig. 4b and compared with the theoretical predictions, to be presented in the following section. The data reveal that the electrical conductance of these MJs is very weakly influenced by single-atom substitution, in agreement with a previous report[35]. In strong contrast, the thermal conductance decreases systematically, as the atomic weight of the substituent increases. We also note that our data reveal that very close to the rupture point (when the junctions are fully stretched), the thermal conductance of *p*BDA junctions reduces to values slightly below those of *p*BDA–F junctions (Supplementary Section 7 provides an additional discussion of the ordering of thermal conductances). This reordering close to the rupture is also reflected in our computations (Supplementary Fig. 27) and is related to the fact that these two molecules feature very similar thermal conductances. The data clearly show that single-atom substitutions enable the independent manipulation of charge and heat transport through MJs.

Insights from first-principles calculations

To understand the origin of the observed attenuation in thermal conductance on adding substituents, we performed detailed ab initio calculations. The calculations are based on the Landauer–Büttiker scattering theory[37–39], which has been used to effectively describe thermal transport through MJs[17,18,28]. We modelled the junctions by connecting the molecule of interest to the Au electrodes and relaxing the resulting geometry to a minimum-energy configuration, ensuring that no net force is applied to the junction (Fig. 5a and Supplementary Fig. 26). We used a top–top geometry in which the Au tips in the calculation form atomically sharp pyramids (Fig. 5a, inset). Next, we stretched the MJs by displacing the electrodes stepwise ($\Delta d = 0.1$ Å near the starting geometry and $\Delta d = 0.005$ Å close to rupture), reoptimizing the junction geometry in each displacement step. In each step, we finally computed the energy-dependent phonon transmission $\tau_{ph}(E)$. This process was repeated until the simulated MJ broke. The computed phonon transmissions for all *p*BDA-derived MJs at a representative displacement of 0.8 Å are shown in Fig. 5a (see also Supplementary Fig. 27). Further, the corresponding cumulative thermal conductance $G^c_{ph}(E)$ (equation (7)), obtained by integrating the transmission up to energy E under the consideration of an appropriate weight function derived from the Bose–Einstein distribution (equation (6)), is presented in Fig. 5a (bottom). Energy ranges that are crucial for differences in thermal conductance are highlighted with orange and brown colours. We note that $G^c_{ph}(E)$ saturates for $E \approx 20$ meV, as no phonon modes are supported in Au above this range. In all linear-response thermal conductance calculations, we assume a temperature of 92 K, corresponding to the average temperature of the electrodes in the experiment. As shown in Fig. 5a, the MJs show a

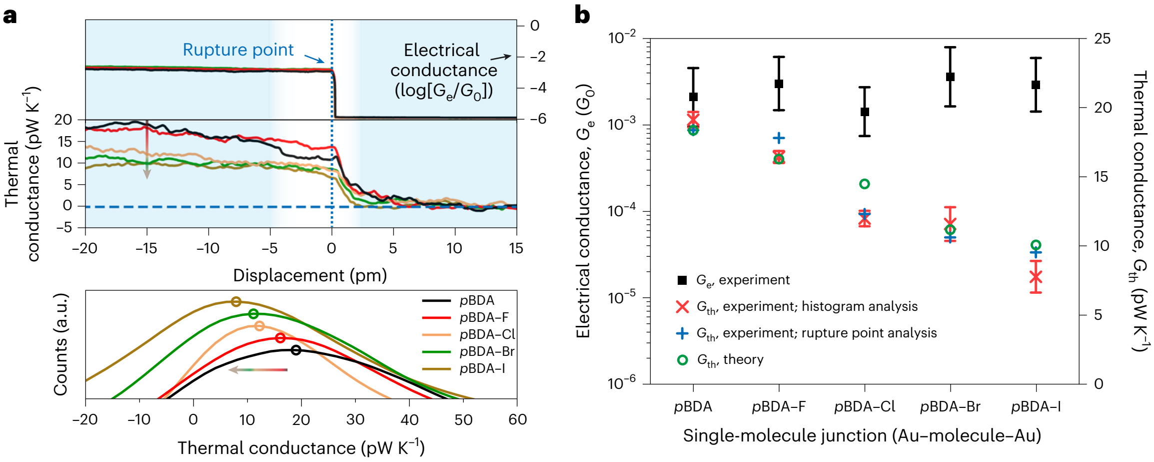

Fig. 4 | Quantification of the effect of substituents on the thermal and electrical transport properties of *p*BDA-derived MJs. a, Comparison of the measured thermal conductances of *p*BDA-derived MJs, using two different analysis approaches (top, rupture point analysis; bottom, histogram analysis). **b**, Summary of the experimental and theoretical results for G_e and G_{th} (experimental results for G_{th} reported from both rupture point analysis and histogram analysis) of *p*BDA-derived MJs. The thermal conductances associated with the rupture point analysis are extracted from the data in **a** at a displacement at −15 pm, which is indicated by the vertical arrow (Supplementary Information provides details of the uncertainty analysis and error estimates for different approaches).

decreasing thermal conductance with increasing substituent mass. We note that the ordering of thermal conductances is rather robust over the whole electrode displacement range with an overall decreasing trend for increasing electrode separation (Supplementary Fig. 27). Averaging over the last 20 pm before junction rupture—resembling the analysis of thermal conductance in terms of the rupture point analysis—results in a good quantitative agreement of theoretically and experimentally determined thermal conductances (Fig. 4b).

The computed $\tau_{ph}(E)$ reveals that the addition of substituents results in two important features: (1) peaks in the transmission of the *p*BDA junction exceeding the value of 1 (see the frequency ranges around 3.5 and 6.5 meV in Fig. 5a) are suppressed on adding substituents, and (2) antiresonances, characterized by a sharp dip in the transmission, are introduced at high energies near 19.0 meV and 16.8 meV for *p*BDA–Br and *p*BDA–I, respectively. The energy at which these antiresonances occur is inversely proportional to the substituent mass[14]. We note that for *p*BDA–F- and *p*BDA–Cl-based MJs, the antiresonances lie above the phonon modes of the highest energy in Au and, therefore, do not influence thermal transport. Overall, the transmission resonances at low energies (feature (1) above) impact the thermal conductance more strongly than the antiresonances (feature (2) above), as low energies have a higher weight in the integral determining the thermal conductance at cryogenic temperatures according to equation (5).

To reveal the underlying transport mechanisms, we developed an eigenmode analysis of phonon transmission eigenchannels (TEs) by generalizing past work[40] (Supplementary Section 9). We note that the TEs are scattering eigenstates that diagonalize the transmission matrix[40] and allow to partition the total transmission into contributions from the orthogonal eigenchannels i, according to $\tau_{ph}(E) = \sum_i \tau_{ph,i}(E)$. Figure 5a (top) shows this decomposition for *p*BDA and *p*BDA–I junctions, where the contributions from the three most transmissive TEs are labelled as $\tau_{ph,\alpha}$, $\tau_{ph,\beta}$ and $\tau_{ph,\gamma}$. To link the TEs to local vibrational properties, we further decompose the wavefunctions of the three TEs α, β and γ into eigenmodes of the central cluster, which consists of the molecule of interest and four Au atoms on each side (Supplementary Section 10). We note that the eigenmodes and eigenmode energies ε_i are energy dependent as the embedding self-energies are included (Supplementary Section 10). The mode coefficients, obtained from this decomposition for the *p*BDA junction, are shown (as examples) for the TEs α and γ in Fig. 5b. We note that for the energy window around 6.5 meV, which features the largest transmission peak (Fig. 5a, top), $\tau_{ph,\alpha}$ is dominated by two eigenmodes with energies ε_1 (6.34 meV) and ε_3 (6.50 meV), whereas $\tau_{ph,\gamma}$ is dominated by eigenmodes with energies ε_2 (6.42 meV) and ε_4 (6.67 meV).

To understand the observed peaks and antiresonances in the transmission functions, we note that the transmission is enhanced if the vibrational modes interfere constructively, whereas the transmission decreases if there is a destructive interference between the modes. The origin of constructive and destructive interferences (as quantified by a propagator analysis, from which we derive simple interference rules (Supplementary Section 10)) can be understood by considering the atomic displacements of the Au atoms that are directly coupled to the electrodes. For example, in Fig. 5c, we illustrate the dominant eigenmodes that contribute to the TE γ of *p*BDA in the vicinity of 6.5 meV. Our analysis (Supplementary Section 10 provides the quantitative details) shows that these eigenmodes interfere constructively, if the displacements of the corresponding atoms in the top and bottom electrodes (corresponding atoms are encoded by identical colours) are parallel in one eigenmode (see the eigenmode shown on the left side of Fig. 5c) and antiparallel in the other (see the eigenmode shown on the right side of Fig. 5c). We find that this constructive interference is sensitive to the energy separation of the eigenmodes (Supplementary Fig. 34).

The origin of antiresonances in the transmission function can be understood by noting that destructive interference arises in the situation, where the displacement of the corresponding atoms in the two relevant eigenmodes is parallel or if the displacement in both eigenmodes is antiparallel. For example, Fig. 5d illustrates the destructive interference arising at around 16.2 meV for TE α in a *p*BDA–I MJ. The relevant eigenmodes (Fig. 5d) clearly show that the displacement of the corresponding Au atom pairs is antiparallel, resulting in the observed antiresonance.

In addition to the effects described above, the characteristics of destructive and constructive interferences are impacted by the symmetry of the interfering eigenmodes (Fig. 5e). In particular, our analysis reveals that on substitution with halogen atoms, the highly symmetric modes of *p*BDA (Fig. 5c) become asymmetric, as reflected by a lower correlation in the direction of motion of the Au atoms at both ends of the molecule (Fig. 5e shows $\tau_{ph,\alpha}$ near 6.5 meV for a *p*BDA–I MJ together with the relevant eigenmodes). The nearest-neighbour harmonic force constants of the C–C bonds, extracted from the density functional theory (DFT) calculations and shown in Fig. 5f, corroborate

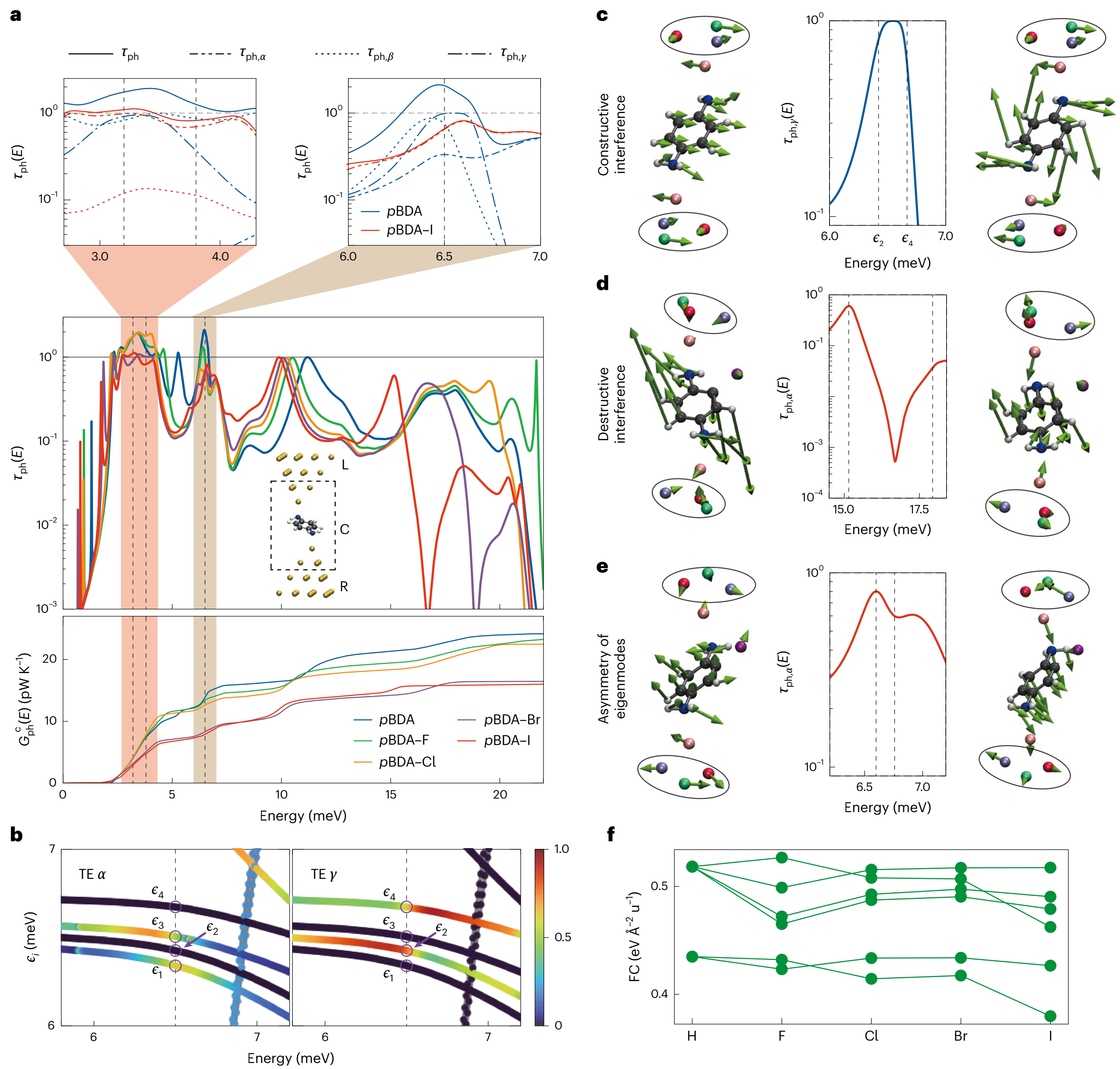

Fig. 5 | Calculated phonon transport for *p*BDA-derived MJs. a, Middle: phonon transmission as a function of energy for all *p*BDA-derived junctions. Top: phonon transmission of *p*BDA and *p*BDA–I MJs in selected energy ranges, resolved into the three most transmissive TEs, namely, α, β and γ. Bottom: cumulative thermal conductances as a function of energy. **b**, Decomposition of the TEs α and γ at a given phonon energy into eigenmodes of the embedded central junction. The chosen energy of 6.5 meV is indicated by the vertical dashed black line with energies ϵ_i of the eigenmodes labelled. The colour coding shows the weight of the contribution of a particular eigenmode to the TE. **c**, TE γ of the *p*BDA MJ shows constructive interference (see also the dash–dotted line in the top-right inset of **a**). The black dashed lines indicate the energies ϵ_2 and ϵ_4 of the interfering modes, identified via the analysis in **b**. The atomic displacements of the eigenmodes are shown on the left and right sides of the plot. **d**, Same data as **c**, but for the destructive interference observed in the *p*BDA–I MJ. **e**, Reduction in the constructive interference in the *p*BDA–I MJ due to the loss of symmetry in vibrational eigenmodes on the substitution of hydrogen by iodine. **f**, Nearest-neighbour force constants (FCs) for out-of-plane coupling for each of the six C–C bonds in the carbon ring.

this further. The force constants of *p*BDA MJs feature doubly and quadruply degenerate values due to the high molecular symmetry, and the addition of halogens notably disrupts these degeneracies. This disruption in symmetry attenuates the constructive interferences for halogen-substituted *p*BDA MJs in the low-energy regions (Fig. 5a), resulting in a lower thermal conductance. The reduction in G_{th} is most pronounced for *p*BDA–Br and *p*BDA–I MJs, for which basically no constructive interferences are observed in the low-energy intervals near 3.5 meV and 6.5 meV.

Outlook

We systematically studied how single-atom substitutions influence the thermal and electrical conductances of MJs. We find that the thermal conductance decreases monotonically with an increasing mass of substituents, achieving a factor-of-two reduction for the substituent with the largest mass (–I). By contrast, the electrical conductance shows no systematic dependence on the substituent mass. We quantitatively explain our observations by developing approaches for describing interactions between the vibrational eigenmodes of MJs. Insights from this work can be potentially applied for tailoring thermal transport in metal–organic frameworks, covalent organic frameworks and molecular thermoelectrics that are of great current interest[11,12,41,42] and rely on transport through molecules. Finally, the experimental advances presented here for probing thermal transport at atomic and molecular scales and at cryogenic temperatures lay the foundation for systematically and precisely exploring heat transport in single-atom wires, polymer chains, 2D materials and quantum devices.

Online content

Any methods, additional references, Nature Portfolio reporting summaries, source data, extended data, supplementary information, acknowledgements, peer review information; details of author contributions and competing interests; and statements of data and code availability are available at https://doi.org/10.1038/s41563-026-02568-9.

References

1. Cahill, D. G. et al. Nanoscale thermal transport. II. 2003-2012. *Appl. Phys. Rev.* **1**, 011305 (2014).
2. Luckyanova, M. N. et al. Coherent phonon heat conduction in superlattices. *Science* **338**, 936–939 (2012).
3. Hochbaum, A. I. et al. Enhanced thermoelectric performance of rough silicon nanowires. *Nature* **451**, 163–167 (2008).
4. Seol, J. H. et al. Two-dimensional phonon transport in supported graphene. *Science* **328**, 213–216 (2010).
5. Qian, X., Zhou, J. W. & Chen, G. Phonon-engineered extreme thermal conductivity materials. *Nat. Mater.* **20**, 1188–1202 (2021).
6. Gehring, P., Thijssen, J. M. & van der Zant, H. S. Single-molecule quantum-transport phenomena in break junctions. *Nat. Rev. Phys.* **1**, 381–396 (2019).
7. Garner, M. H. et al. Comprehensive suppression of single-molecule conductance using destructive σ-interference. *Nature* **558**, 415–419 (2018).
8. Xu, B. & Tao, N. Measurement of single-molecule resistance by repeated formation of molecular junctions. *Science* **301**, 1221–1223 (2003).
9. Diercks, C. S. & Yaghi, O. M. The atom, the molecule, and the covalent organic framework. *Science* **355**, 923–931 (2017).
10. Evans, A. M. et al. Thermally conductive ultra-low dielectric layers based on two-dimensional covalent organic frameworks. *Nat. Mater.* **20**, 1142–1148 (2021).
11. Mohseni, M. M. et al. Metal-organic frameworks (MOF) based heat transfer: a comprehensive review. *Chem. Eng. J.* **449**, 137700 (2022).
12. Furukawa, H., Cordova, K. E., O'Keeffe, M. & Yaghi, O. M. The chemistry and applications of metal-organic frameworks. *Science* **341**, 1230444 (2013).
13. Famili, M., Grace, I., Sadeghi, H. & Lambert, C. J. Suppression of phonon transport in molecular Christmas trees. *ChemPhysChem* **18**, 1234–1241 (2017).
14. Klöckner, J.-C., Cuevas, J. C. & Pauly, F. Tuning the thermal conductance of molecular junctions with interference effects. *Phys. Rev. B* **96**, 245419 (2017).
15. Bro-Jørgensen, W., Bay-Smidt, A. J., Donadio, D. & Solomon, G. C. Heavy solution for molecular thermal management: phonon transport suppression with heavy atoms. *ACS Phys. Chem. Au.* **5**, 162–170 (2024).
16. Blaschke, M. & Pauly, F. Revealing molecule-internal mechanisms that control phonon heat transport through single-molecule junctions by a genetic algorithm. *ACS Nano* **19**, 32093–32107 (2025).
17. Cui, L. et al. Thermal conductance of single-molecule junctions. *Nature* **572**, 628–633 (2019).
18. Mosso, N. et al. Thermal transport through single-molecule junctions. *Nano Lett.* **19**, 7614–7622 (2019).
19. Greenwald, J. E. et al. Highly nonlinear transport across single-molecule junctions via destructive quantum interference. *Nat. Nanotechnol.* **16**, 313–317 (2021).
20. Guédon, C. M. et al. Observation of quantum interference in molecular charge transport. *Nat. Nanotechnol.* **7**, 305–309 (2012).
21. Frisenda, R., Janssen, V. A., Grozema, F. C., van der Zant, H. S. & Renaud, N. Mechanically controlled quantum interference in individual π-stacked dimers. *Nat. Chem.* **8**, 1099–1104 (2016).
22. Yelishala, S. C. et al. Phonon interference in single-molecule junctions. *Nat. Mater.* **24**, 1258–1264 (2025).
23. Li, Y. et al. Gate controlling of quantum interference and direct observation of anti-resonances in single molecule charge transport. *Nat. Mater.* **18**, 357–363 (2019).
24. Bai, J. et al. Anti-resonance features of destructive quantum interference in single-molecule thiophene junctions achieved by electrochemical gating. *Nat. Mater.* **18**, 364–369 (2019).
25. Markussen, T. & Thygesen, K. S. Temperature effects on quantum interference in molecular junctions. *Phys. Rev. B* **89**, 085420 (2014).
26. Dubi, Y. & Di Ventra, M. Colloquium: heat flow and thermoelectricity in atomic and molecular junctions. *Rev. Mod. Phys.* **83**, 131–155 (2011).
27. Gotsmann, B., Gemma, A. & Segal, D. Quantum phonon transport through channels and molecules—a perspective. *Appl. Phys. Lett.* **120**, 160503 (2022).
28. Cui, L. et al. Quantized thermal transport in single-atom junctions. *Science* **355**, 1192–1195 (2017).
29. Nguyen, T. et al. Niobium nitride thin films for very low temperature resistive thermometry. *J. Low Temp. Phys.* **197**, 348–356 (2019).
30. Bourgeois, O., André, E., Macovei, C. & Chaussy, J. Liquid nitrogen to room-temperature thermometry using niobium nitride thin films. *Rev. Sci. Instrum.* **77**, 126108 (2006).
31. Dechaumphai, E. & Chen, R. Sub-picowatt resolution calorimetry with niobium nitride thin-film thermometer. *Rev. Sci. Instrum.* **85**, 094903 (2014).
32. López-Nebreda, R. et al. Heat transfer in metallic nanometre-sized gaps. *Nat. Commun.* **16**, 7342 (2025).
33. Gemma, A. et al. Full thermoelectric characterization of a single molecule. *Nat. Commun.* **14**, 3868 (2023).
34. Chen, W. et al. Highly conducting π-conjugated molecular junctions covalently bonded to gold electrodes. *J. Am. Chem. Soc.* **133**, 17160–17163 (2011).
35. Venkataraman, L. et al. Electronics and chemistry: varying single-molecule junction conductance using chemical substituents. *Nano Lett.* **7**, 502–506 (2007).
36. Marder, M. P. *Condensed Matter Physics* (John Wiley & Sons, 2010).
37. Cuevas, J. C. & Scheer, E. *Molecular Electronics: An Introduction To Theory And Experiment* 2nd edn (World Scientific, 2017).
38. Li, N. et al. *Colloquium*: phononics: manipulating heat flow with electronic analogs and beyond. *Rev. Mod. Phys.* **84**, 1045–1066 (2012).
39. Wang, J. J., Gong, J., McGaughey, A. J. H. & Segal, D. Simulations of heat transport in single-molecule junctions: investigations of the thermal diode effect. *J. Chem. Phys.* **157**, 174105 (2022).
40. Klöckner, J. C., Cuevas, J. C. & Pauly, F. Transmission eigenchannels for coherent phonon transport. *Phys. Rev. B* **97**, 155432 (2018).
41. Kwon, J. et al. Thermal conductivity of covalent-organic frameworks. *ACS Nano* **17**, 15222–15230 (2023).
42. Gemma, A. & Gotsmann, B. A roadmap for molecular thermoelectricity. *Nat. Nanotechnol.* **16**, 1299–1301 (2021).

Methods

Fabrication of CSPs

The fabrication steps (Supplementary Section 2) for the CSPs used in this work are shown in Supplementary Fig. 3a. Briefly, T-beams were first defined on a bare Si wafer using a deep reactive ion etching method, followed by a low-pressure chemical vapour deposition of 600 nm of low-stress silicon nitride. Next, a 30-nm-thick serpentine platinum (Pt) line, a 70-nm-thick Au line and a 100-nm niobium nitride film were patterned (Fig. 1b). After that, Au electrodes (500 nm thick) for wire bonding were electron-beam evaporated. Subsequently, the suspended structure was created and released via backside reactive ion etching of the silicon nitride and deep reactive ion etching of the silicon. After releasing the suspended structure (Supplementary Fig. 3b), the probe was thoroughly cleaned in a Piranha solution and transferred to a focused ion beam system (Helios 650) to attach a single-crystal Au wire with the help of an integrated micromanipulator. Approximately 200 nm of Pt were deposited at the interface of the attached Au wire and the Au surface of the probe to create a good electrical and thermal connection between the Au surface and the Au wire. Finally, the attached Au wire was further sharpened using a focused ion beam to achieve a tip radius of ~10 nm (Supplementary Fig. 3c shows a CSP with an attached sharpened Au wire after step 8).

Measurement of electrical conductance of atomic and molecular junctions

As shown in Fig. 1b and Supplementary Fig. 8, a high-frequency (1,001 Hz) sinusoidal voltage ($V_{\text{bias}} = 5$ mV), sourced from a wavefunction generator (Hewlett Packard 33120A), was applied to the substrate's Au electrode. During the experiments, when a junction was formed between the two Au electrodes, an electrical current (I_e) started to flow through the junction and was converted to a voltage signal (V_e) using a current-to-voltage amplifier (DLPCA200). The voltage signal was then measured via a lock-in amplifier (SR830, SRS) with a time constant of 10 ms, which corresponds to an equivalent bandwidth of approximately 15.6 Hz. Subsequently, the electrical conductance of the junction (G_e) was calculated as follows (Supplementary Section 4):

$$G_{\text{e}} = \frac{1}{R_{\text{e}}} = \left(\frac{V_{\text{bias}}}{I_{\text{e}}} - R_{\text{e},0}\right)^{-1}. \tag{1}$$

We note that here the amplitude of V_{bias} was chosen to be 5 mV to ensure that the Joule heat generated by the electrical current (I_e) was negligible in the thermal measurements for both Au junctions and MJs (Supplementary Section 4 provides the analysis of Joule heat dissipated in the junctions). The impact of Joule heating on the measured thermal conductance of the Au and MJs was approximately 0.2 pW K^{-1} and 0.02 pW K^{-1}, respectively. These values are <1% of the measured thermal conductance of the Au junctions (~170 pW K^{-1}) and MJs (~10–20 pW K^{-1}) and, hence, negligible.

Measurement of thermal conductance of atomic and molecular junctions

To measure the thermal conductance of the junctions, a d.c. current ($I_{\text{Pt,d.c.}}$ = ~110 μA) was applied to the integrated Pt line to raise the temperature of the CSP by ~30 K (that is, T_p = ~107 K; Supplementary Fig. 9). During the measurements, when a junction was formed between the two Au electrodes, the thermal pathway created by the junction resulted in a temperature change (ΔT_p) of the CSP on the order of millikelvin. This temperature change in the CSP was detected by the resistance change in the NbN$_x$ thermometer ($\Delta R_{\text{NbN}x}(\Delta T_p)$), which was measured using a half-bridge (Supplementary Fig. 9 and Supplementary Section 4). The thermal conductance of the junctions (G_{th}) was determined as

$$G_{\text{th}} = \frac{1}{R_{\text{th,j}}} = \frac{\Delta T_{\text{p}}(1 - \alpha_{\text{Pt}}(T_{\text{p}} - T_0))}{R_{\text{th,probe}}(T_{\text{p}} - T_0)}, \tag{2}$$

where T_0 is the environmental temperature (77 K), α_{Pt} is the temperature coefficient of resistance of the platinum line and $R_{\text{th,probe}}$ is the thermal resistance of the CSP, that is, the reciprocal of the measured thermal conductance of the probe ($G_{\text{th,probe}}$). We note that the amplitude and frequency of the sensing current ($I_{\text{NbN}x}$) were carefully chosen to obtain a good signal-to-noise ratio for thermal measurements and to minimize Joule heating and displacements of the two electrodes due to the modulated thermal expansion.

Cleaning protocol for achieving a negligible background thermal conductance

On careful experimentation, we identified that a negligible background thermal conductance can be accomplished by (1) the incorporation of a nanometrically sharp metallic tip, which reduces near-field thermal radiation and the amount of surface area, across which molecules can potentially bridge the tip and the substrate; (2) precleaning the Au tip using an ion beam and ensuring that the Au substrate is clean before coating it with the studied molecules (Supplementary Section 1 shows how this is done); (3) locally cleaning a patch of Au on the substrate by exposing a microscopically small area by gently pushing the Au tip into the Au substrate and retracting the tip to expose pristine Au; and (4) performing experiments in an ultrahigh-vacuum environment and at cryogenic temperatures (for example, 77 K). Operation at cryogenic temperatures suppresses the surface diffusion of molecules, thereby keeping the pristine Au region (created by poking the tip into the substrate) free from accumulating many molecules and enabling the trapping of a single molecule. Further, the ultrahigh-vacuum and low-temperature environments suppress thermal transport by residual gas molecules and by near-field thermal radiation to negligible levels. Following this protocol enabled us to achieve negligible background conductance on all the samples that we prepared, that is, all measurements were performed with a negligible thermal conductance background.

Selection criteria for junction traces

For each of the studied molecules, approximately 1,500 traces were collected (~1,500 traces out of 10,000 approach–withdrawal cycles showing the formation of single-molecule junctions). All 1,500 traces were used in our histogram analysis (Fig. 2b and Supplementary Figs. 18a–b, 19b–d and 20 show the representative traces used in our data analysis, which featured a sharp or a gradual change in the electrical conductance when the MJs ruptured; Supplementary Sections 5–7). Out of these 1,500 traces, ~300 traces feature a rapid change in the electrical conductance of the MJs, signalling an abrupt rupture of a single-molecule junction, which was identified objectively using an automated code. These ~300 traces were used in the rupture point analysis.

Theoretical modelling

Phonon heat transport. Phononic transport properties are calculated within the Landauer–Büttiker scattering theory using non-equilibrium Green's function techniques[37,43,44]. The phonon transmission is determined by

$$\tau_{\text{ph}}(E) = \text{Tr}[D^{\text{r}}_{\text{CC}}(E)\Lambda_{\text{L}}(E)D^{\text{a}}_{\text{CC}}(E)\Lambda_{\text{R}}(E)]. \tag{3}$$

Here $\Lambda_X(E) = \text{i}\left[\Pi^{\text{r}}_X(E) - \Pi^{\text{a}}_X(E)\right]$ is the linewidth broadening matrix of electrode $X = \text{L}, \text{R}$, which is related to the embedding self-energy $\Pi^{\text{r}}_{\text{X}}(E)$, and $D^{\text{r}}_{\text{CC}}(E) = [D^{\text{a}}_{\text{CC}}(E)]^{\dagger}$ is the retarded Green's function of the central junction part[44]:

$$D^{\text{r}}_{\text{CC}}(E) = \left[(E + \text{i}\eta)^2 - K_{\text{CC}} - \Pi^{\text{r}}_{\text{L}}(E) - \Pi^{\text{r}}_{\text{R}}(E)\right]^{-1}. \tag{4}$$

In this expression, K_{CC} is the dynamical matrix (or mass-scaled Hessian) of the central part. The phonon thermal conductance is calculated using

$$G_{\text{ph}}(T) = \kappa_0 \int_0^{\infty} \text{d}E W_{\text{ph}}(E, T)\tau_{\text{ph}}(E), \tag{5}$$

where $\kappa_0 = \pi^2 k_B{}^2 T/(3h)$ and $W_{ph}(E,T)$ is an energy- and temperature-dependent weight function containing the Bose–Einstein distribution $n(E,T)$ (ref. 45):

$$W_{ph}(E,T) = \frac{3}{\pi^2}\left(\frac{E}{k_B T}\right)^2 \left(-\frac{\partial n(E,T)}{\partial E}\right). \tag{6}$$

Note that the weight function is normalized as $\int_0^\infty dE\, W_{ph}(E,T) = 1$, and further properties of $W_{ph}(E,T)$ are discussed in past work[45]. To resolve the contributions of individual transmission peaks to $G_{ph}(T)$, the cumulative thermal conductance

$$G^c_{ph}(E) = \kappa_0 \int_0^E dE'\, W_{ph}(E',T)\tau_{ph}(E') \frac{\partial n(E',T)}{\partial E'} \tag{7}$$

is analysed.

Electronic structure calculations. The information needed in the phonon transport formalism, namely, the Hessian matrix of the junction geometry, is extracted from DFT calculations using TURBOMOLE (v. 7.7)[46]. We use the def-SV(P) Gaussian basis set[47–49] for all atoms with the corresponding Coulomb fitting basis. The Perdew–Burke–Ernzerhof exchange–correlation functional[50,51] is used in all calculations. Total energies are converged to better than 10^{-7} a.u. ('scfconv 7'), and geometries are relaxed until the gradient norm is below 10^{-5} a.u. ('gcart 5'). We furthermore apply the DFT-D3 dispersion correction with Becke–Johnson damping ('disp3 -bj')[52].

Construction of junction geometries. We model the junction geometry via a so-called extended central cluster. For this, the energy-optimized isolated molecule is connected to tetrahedral Au pyramids, each consisting of 20 Au atoms on the left and right sides. To stabilize the system and provide a fixed junction length, the back layers of the Au pyramids are fixed. We allow the top four Au atoms on each side that are closest to the molecule and the molecule itself to adjust their position during energy optimization. The Au clusters that mimic the electrode tips are (in their unrelaxed form) related to each other by an inversion centre in the middle of the junction. Seen along the transport direction, the fixed Au atoms resemble a perfect face-centred-cubic lattice structure, oriented along the (111) crystallographic axis. In the transport calculations, the fixed Au atoms are regarded as part of semi-infinite Au electrodes to accurately describe the transport properties of the junction. These well-established theoretical methods have been described in previous work[44,53] (Supplementary Information).

Determination of phonon thermal conductances. To compare the computational data with the experimental data in Fig. 4b, we also apply the rupture point analysis to the computational data. Specifically, we average the distance-dependent thermal conductance traces obtained from our calculations for each MJ over a 20-pm range before the rupture point. Note that we neglect the electrical contribution to the thermal conductance, since it is expected to be smaller than 1 pW K^{-1} based on the Wiedemann–Franz law[36].

Data availability

All data supporting the findings of this study are available in the Article and its Supplementary Information. These data are also available via figshare (https://doi.org/10.6084/m9.figshare.31383004)[54] as well as from the corresponding authors.

Code availability

The DFT program used to determine the junction geometries and analyse the vibrational properties is available from www.turbomole.com. The corresponding custom-developed code for the description of phonon transport implements the procedures outlined in ref. 44 and is available from F.P. on request.

References

43. Wang, J.-S., Wang, J. & Lü, J. Quantum thermal transport in nanostructures. *Eur. Phys. J. B* **62**, 381–404 (2008).
44. Bürkle, M., Hellmuth, T. J., Pauly, F. & Asai, Y. First-principles calculation of the thermoelectric figure of merit for [2, 2] paracyclophane-based single-molecule junctions. *Phys. Rev. B* **91**, 165419 (2015).
45. Klöckner, J. C., Matt, M., Nielaba, P., Pauly, F. & Cuevas, J. C. Thermal conductance of metallic atomic-size contacts: phonon transport and Wiedemann-Franz law. *Phys. Rev. B* **96**, 205405 (2017).
46. Franzke, Y. J. et al. TURBOMOLE: today and tomorrow. *J. Chem. Theory Comput.* **19**, 6859–6890 (2023).
47. Schäfer, A., Horn, H. & Ahlrichs, R. Fully optimized contracted Gaussian basis sets for atoms Li to Kr. *J. Chem. Phys.* **97**, 2571–2577 (1992).
48. Eichkorn, K., Weigend, F., Treutler, O. & Ahlrichs, R. Auxiliary basis sets for main row atoms and transition metals and their use to approximate Coulomb potentials. *Theor. Chem. Acta.* **97**, 119–124 (1997).
49. Eichkorn, K., Treutler, O., Öhm, H., Häser, M. & Ahlrichs, R. Auxiliary basis sets to approximate Coulomb potentials. *Chem. Phys. Lett.* **240**, 283–290 (1995).
50. Perdew, J. P. & Wang, Y. Accurate and simple analytic representation of the electron-gas correlation energy. *Phys. Rev. B* **45**, 13244 (1992).
51. Perdew, J. P., Burke, K. & Ernzerhof, M. Generalized gradient approximation made simple. *Phys. Rev. Lett.* **77**, 3865 (1996).
52. Grimme, S., Ehrlich, S. & Goerigk, L. Effect of the damping function in dispersion corrected density functional theory. *J. Comput. Chem.* **32**, 1456–1465 (2011).
53. Pauly, F. et al. Cluster-based density-functional approach to quantum transport through molecular and atomic contacts. *New J. Phys.* **10**, 125019 (2008).
54. Luan Y. et al. Tuning phonon transmission via single-atom substituents. *figshare* https://doi.org/10.6084/m9.figshare.31383004 (2026).

Acknowledgements

We thank the Lurie Nanofabrication Facility and the Michigan Center for Materials Characterization for facilitating the fabrication and calibration of devices. E.M. and P.R. acknowledge support from the Department of Energy (Basic Energy Sciences award number DE-SC0004871, development of scanning calorimetric probes) and the Office of Naval Research (award number N00014-24-1-2132, instrumentation). P.R. thanks the Army Research Office for support (award number W911NF2310260, materials characterization). F.P. gratefully acknowledges funding by the German Research Foundation (Deutsche Forschungsgemeinschaft) within the Collaborative Research Center (Sonderforschungsbereich) 1585 (project number 492723217), subproject C02 and acknowledges use of the LiCCA high-performance computing cluster of the University of Augsburg, co-funded by the German Research Foundation (project number 499211671).

Author contributions

F.P., E.M. and P.R. conceived and supervised the project. Y.L., Y.I. and J.G. fabricated the CSPs and characterized the probe properties. Y.L., E.M. and P.R. designed the experimental method used in this work. Y.L. conducted all the experiments. Y.L. and Y.I. analysed the experimental data. M.B. and F.P. performed the theoretical modelling. M.B. carried out all the theoretical calculations and analysed the computational results. The manuscript was written by Y.L., M.B., F.P., E.M. and P.R., with comments and input from all authors.

Competing interests

The authors declare no competing interests.

Additional information

Supplementary information The online version contains supplementary material available at https://doi.org/10.1038/s41563-026-02568-9.

Correspondence and requests for materials should be addressed to Fabian Pauly, Edgar Meyhofer or Pramod Reddy.

Peer review information *Nature Materials* thanks Renkun Chen and the other, anonymous, reviewer(s) for their contribution to the peer review of this work.